nature communications

Article

https://doi.org/10.1038/s41467-025-65083-6

Measuring Hall voltage and Hall resistance in an atom-based quantum simulator

Received: 13 December 2024

Accepted: 4 October 2025

Published online: 21 November 2025

Check for updates

T.-W. Zhou[1], T. Beller[1], G. Masini[2], J. Parravicini[1,2,3], G. Cappellini[2,3], C. Repellin[4], T. Giamarchi[5], J. Catani[2,3], M. Filippone[6] & L. Fallani[1,2,3]

In the Hall effect, a voltage drop develops perpendicularly to the current flow in the presence of a magnetic field, leading to a transverse Hall resistance. Recent developments with quantum simulators have unveiled strongly correlated and universal manifestations of the Hall effect. However, a direct measurement of the Hall voltage and of the Hall resistance in a non-electronic system of strongly interacting fermions was not achieved to date. Here, we demonstrate a technique for measuring the Hall voltage in a neutral-atom-based quantum simulator. From that we provide the first direct measurement of the Hall resistance in a cold-atom analogue of a solid-state Hall bar and study its dependence on the carrier density, along with theoretical analyses. Our work closes a major gap between analogue quantum simulations and measurements performed in solid-state systems, providing a key tool for the exploration of the Hall effect in highly tunable and strongly correlated systems.

The Hall effect[1–4] is a macroscopic manifestation of the Lorentz force exerted by a magnetic field on the charge carriers of a conductor. In normal conductors threaded by a magnetic field B, the Hall effect manifests itself as a voltage drop corresponding to the emergence of an electric field E_y, perpendicular to the current density flow j_x. The ratio between these two quantities defines the Hall resistivity

$$\rho_{\mathrm{H}} = \frac{E_y}{j_x}. \tag{1}$$

Despite its simple origin, the study of this quantity has played a central role for the exploration and understanding of solid-state systems[5,6]. For small magnetic fields, within semiclassical approximations, the Hall resistivity ρ_{H} is proportional to $-B/nq$ and measures the inverse of the carrier density n and their charge q. The observation of a negative Hall resistivity has been an early signature of electrical conduction by holes before the advent of band theory[1]. The study of the Hall effect under the action of strong magnetic fields has led to the discovery of the integer[7] and fractional[8] quantum Hall effects, where $1/\rho_{\mathrm{H}}$ is exactly quantized in units and fractions of the universal constant e^2/h. The study of such phenomena has subsequently fostered the entire field of topological quantum matter[9–13].

However, understanding the Hall effect has remained challenging whenever interactions are present among the carriers. The quest for further insight[14–16] has motivated an intense experimental work in the last decade, with the realization of analogue quantum simulators exploiting ultracold atoms subjected to artificial magnetic fields[17–29] and circuit quantum electrodynamics[16,30].

Recent experiments with cold atoms[27,31] have measured the transverse polarization in synthetic flux ladders after inducing a transient longitudinal current, revealing a universal behavior above an interaction threshold[27,32]. A precursor signature of the topological robustness of ρ_{H} for insulating phases has also been probed through Středa's formula[26]. In normal conductors, the robustness of the connection between the Hall resistance and the inverse carrier density is deeply rooted in Galilean invariance[33,34]. However, despite being a natural quantity of easy access in the solid state, the transport measurement of the Hall resistance in a neutral system such as an

[1]Department of Physics and Astronomy, University of Florence, 50019 Sesto Fiorentino, Italy. [2]European Laboratory for Non-Linear Spectroscopy (LENS), 50019 Sesto Fiorentino, Italy. [3]Istituto Nazionale di Ottica del Consiglio Nazionale delle Ricerche (CNR-INO), Sezione di Sesto Fiorentino, 50019 Sesto Fiorentino, Italy. [4]Université Grenoble Alpes, CNRS, LPMMC, 38000 Grenoble, France. [5]Department of Quantum Matter Physics, University of Geneva, 1211 Geneva, Switzerland. [6]Université Grenoble Alpes, CEA, IRIG-MEM-L_SIM, 38000 Grenoble, France. e-mail: fallani@lens.unifi.it

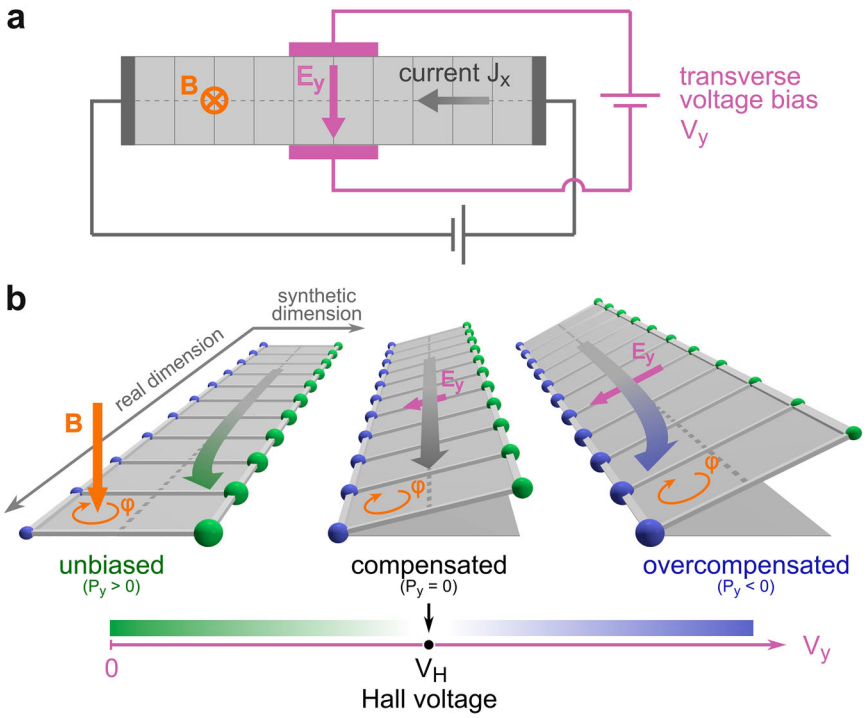

Fig. 1 | Measuring electrical quantities in a synthetic Hall bar. a An analogue quantum simulation of a Hall bar is realized by trapping ultracold atoms in ladder geometries. An atomic current J_x is subjected to a perpendicular effective magnetic field B and to synthetic electric fields realized by energy gradients along both the longitudinal direction ($\hat{x}$) and the transverse direction ($\hat{y}$, encoded in the internal spin state according to the concept of synthetic dimension). **b** The transverse voltage bias that compensates the bending of the carrier trajectories induced by the Hall effect (measured by the spin polarization P_y) provides a direct measurement of the Hall voltage V_H, from which the Hall resistance is extracted.

atomic quantum simulator has remained out of reach so far. Such a measurement would permit the unprecedented investigations of the Hall response of strongly correlated conductors, bringing new input to the theoretical challenge[35–43] of understanding anomalous temperature dependence and sign changes of ρ_H in correlated solid-state systems[44–48].

In this work, we demonstrate a quench protocol to measure the Hall resistance in a Hall bar of strongly interacting ultracold fermions, which generalizes the theoretical protocol of ref. 49 to finite magnetic fields. Our method is based on the tracking of the transverse polarization along the bar, and on the application of a controlled effective voltage bias in the transverse direction to compensate it. By controlling the number of particles in the system and the transverse size of the system, we provide direct experimental evidence of the predicted $1/n$ dependence of the Hall resistance (1) on the carrier density n, irrespective of the microscopic details of the system. We also provide the theoretical demonstration that such behavior is stabilized by strong repulsive interactions in ladder systems and that it is a manifestation of the universal Hall response of single-band metals[27,32]. Our experiment reproduces the electrical measurements performed on solid-state Hall devices and lays the foundations for the investigation of the quantum Hall effect and, more generally, of topologically protected transport in strongly correlated systems.

Results

Quantum simulation of a Hall bar

Our experiment operates with ultracold Fermi gases of ^{173}Yb atoms trapped in a deep 2D optical lattice, resulting in an array of fermionic 1D quantum wires (in the following called "tubes") along the $\hat{x}$-direction. We engineer Hall bars in the form of synthetic ladders, where the dynamics along the longitudinal direction are controlled by an additional optical lattice along $\hat{x}$. The nuclear-spin states of the atoms act as different sites along a synthetic dimension $\hat{y}$, which provides the transverse direction of the ladder[20,27], see Fig. 1. The plaquettes of the ladder are threaded by a synthetic magnetic flux φ, generated by phase imprinting by Raman lasers coupling the different spin states, which simulates the action of a magnetic field B perpendicular to the Hall bar (see Methods for details about the experiment). We realize two- and three-leg ladder systems where a current J_x along the longitudinal $\hat{x}$-direction is induced by an energy gradient along the same direction, which is equivalent to applying a longitudinal electric field E_x (see Fig. 1). The Hall effect is signaled by the emergence of a transverse density polarization of the system P_y[32,50]. Here we directly measure the transverse Hall voltage V_H caused by this polarization, by applying an energy offset between the legs of the ladder, so as to mimic the effect of a transverse electric field E_y (see following section), and adjusting it such that $P_y = 0$, see Figs. 1 and 2. Such a measurement of E_y allows us to derive the reactive Hall resistance[39,49,51].

The system, prior to the quench protocol of activating the longitudinal current and the transverse field, can be described by the interacting Harper-Hofstadter Hamiltonian

$$H = -t_x \sum_{j,m} \left[a^\dagger_{j,m} a_{j+1,m} + \text{h.c.} \right] + \frac{U}{2} \sum_{j,m,m' \neq m} n_{j,m} n_{j,m'} - t_y \sum_{j,m} \left[e^{i\varphi j} a^\dagger_{j,m} a_{j,m+1} + \text{h.c.} \right], \quad (2)$$

where $a_{j,m}$ and $a^\dagger_{j,m}$ are fermionic annihilation and creation operators acting on site (j, m), $n_{j,m} = a^\dagger_{j,m} a_{j,m}$ and h.c. is the Hermitian conjugate operator. The lattice label j corresponds to the real $\hat{x}$-dimension, while the labels m, $m' \in [1, M]$ indicate the synthetic $\hat{y}$-dimension with $M = 2$ or 3, corresponding to the nuclear spin states $m_F = -5/2$, $-1/2$ and $+3/2$. Here, t_x is the nearest-neighbor tunneling amplitude and U is the "on-rung" repulsive interaction energy between two atoms with different nuclear spin in the same real-lattice site and with global SU(M) interaction symmetry[52]. The dynamics along the synthetic dimension is

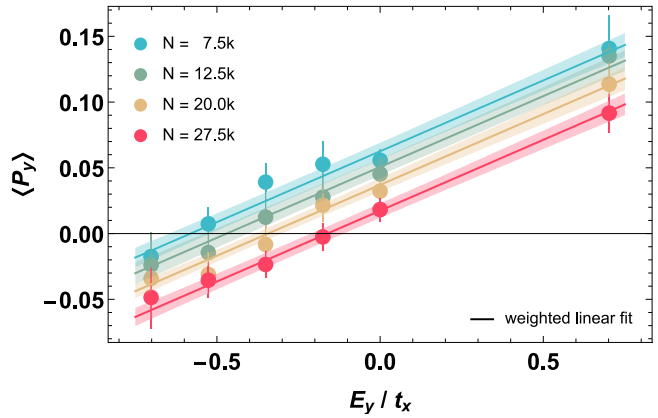

Fig. 2 | Measurement of the Hall voltage. The time-averaged Hall polarization $\langle P_y\rangle$ for two-leg ladders, measured at $t_y = 3.30t_x$ and $U = 6.56t_x$, is shown as a function of the transverse field E_y with different total atom number N; the error bars depict the standard error of the mean and are obtained with a statistical Bootstrap method. The solid lines in corresponding colors are obtained from a weighted global linear fit based on the error bars of the experimental data, while color shades represent the 95% confidence bands of the fit.

encoded in the complex hopping amplitude $t_y e^{i\varphi j}$, whereby the position-dependent phase simulates the effect of a static magnetic flux $\varphi = 0.32\pi$ threading a plaquette of the ladder (see "Methods").

In the non-interacting limit ($U = 0$), the single particle spectrum of Eq. (2) is composed of M independent conduction bands. However, the strong repulsion among the nuclear spin states stabilizes a single-band correlated metal, whose hallmark in the two-leg case was shown to be a universal Hall imbalance $\Delta_H = P_y/J_x = 2t_x \tan(\varphi/2)/t_y$, robust to variations of particle densities, confinement, finite temperatures, and strong drives[27]. We will show that such behavior in the universal single-band regime underpins the observation of the universal scaling with $1/n$ of the Hall resistance[32,49], and also extends to a three-leg ladder.

Experimental protocol

The experiment is performed in the universal single-band regime at $t_y = 3.30t_x$ and $U = 6.56t_x$[27]. A light-shift gradient, which results in the additional Hamiltonian term $H_x = E_x\sum_{j,m} j n_{j,m}$ ($E_x = 0.5t_x$), tilts the ladder in the real-lattice direction and thus generates a current along $\hat{x}$ (see Methods). After E_x is instantaneously activated, the longitudinal current $J_x(\tau) = 2t_x \int_{-1}^{1} \sin(\pi k) n(k,\tau)\mathrm{d}k$ is accessed by measuring the total lattice momentum distribution $n(k, \tau)$ with a band-mapping technique[27], where τ is defined in units of $\hbar/t_x$ and $\hbar$ is the reduced Planck's constant. The momentum distribution is normalized to the total atom number $N = \int_{-1}^{1} n(k)\mathrm{d}k$, and the lattice momenta k are expressed in units of the real-lattice wavenumber $k_L = \pi/d$, with the lattice spacing $d = 380$ nm. The induced transverse Hall polarization P_y is evaluated as a difference in the fractional spin population, with respect to the starting value at $\tau = 0$, namely: $P_y(\tau) = [N_M(\tau) - N_1(\tau)]/N(\tau) - [N_M(0) - N_1(0)]/N(0)$[27]. The atom number N_m in spin state m is measured by performing an optical Stern-Gerlach detection[53]. To compensate this induced polarization P_y, we employ a synthetic gradient realized by controlling the detuning of the Raman coupling (see Methods), equivalent to an external potential term $H_y = -E_y\sum_{j,m} m\, n_{j,m}$, which is activated together with H_x. We determine the Hall voltage V_H, by adjusting E_y to suitable values such that the time average of the polarization vanishes, i.e., $\langle P_y\rangle = \langle P_y(\tau)\rangle_\tau = 0$ in the time interval $\tau \in [1, 5]$, for which we have already verified in ref. 27 that the Hall response reaches a stationary universal value. We label this fine-tuned field E_H. It can be immediately put in relation with the Hall voltage by multiplying it by the total number of legs $V_H = -(M-1)E_H$. Notice that, for the case with two legs, these two quantities coincide. In Fig. 2 we show the dependence of $\langle P_y\rangle$ over E_y for a set of different total atom numbers, used to retrieve the values of the Hall voltage as a function of N, as discussed in the following sections.

Theoretical background

This experimental procedure differs from protocols proposing to measure ρ_H either in stationary regimes[32,39,50,51] or to fine-tune E_y such to suppress the polarization P_y at every single time[49], and presents the advantage compared to the proposed protocol of ref. 49 to work for finite magnetic fields and not just in the limit of $B \to 0$, allowing us to extract a sizeable Hall signal from the experiment. In the Supplementary Information, we show that, regardless of the experimental procedure, for an ideal system – at zero temperature, infinite and perfectly periodic – in the single-band metal regime, the polarization P_y and the current J_x are bound by the relation

$$\langle P_y\rangle = \left(E_y - 2\tan\left(\frac{\varphi}{2}\right)\frac{\langle J_x\rangle}{N}\right)\mathcal{I}_M, \tag{3}$$

where only the proportionality constant $\mathcal{I}_M$ depends on the number of legs M ($\mathcal{I}_2 = 1/(2t_y)$ and $\mathcal{I}_3 = \sqrt{2}/t_y$, see also ref. 32, which addressed exclusively the $\varphi \to 0$ limit). Additionally, assuming that it is possible to fine-tune E_y to a value E_H such that $\langle P_y\rangle = 0$, one finds the universal relation

$$\rho_H = \frac{E_H}{\langle J_x\rangle} = \frac{2}{N}\tan\left(\frac{\varphi}{2}\right). \tag{4}$$

Equations (3) and (4) feature the total number of atoms N, because our experiment can only access global quantities, instead of the current and polarization densities in each tube. We show in the Supplementary Information that such relations reflect the intimate connection between ρ_H and the inverse carrier density $1/n$ in each tube. Notice that, as a sign of the universality of the Hall effect, the relation (4) between E_H and J_x does not depend on any microscopic detail of the system, apart from the number of carriers N and the magnetic flux φ. This is not the case for P_y, which depends on the microscopic structure through the factor $\mathcal{I}_M$.

We stress that the presence of strong repulsions in the system is key to stabilize a strongly correlated single-band metal[27,32,50,54] and, consequently, the universal scaling Eq. (4), as we are going to observe in our experimental setup.

Demonstration of the $1/n$ scaling of ρ_H

To measure the Hall resistance, we first inspect the behavior of $\langle P_y\rangle$ in the case of a two-leg ladder, realized upon the nuclear spin states $m_F = -1/2$ and $m_F = -5/2$. Figure 2 reports the dependence of $\langle P_y\rangle$ as a function of the transverse field E_y, for different atom numbers $N = 7.5$ k, 12.5 k, 20.0 k, and 27.5 k. Accordingly to the constitutive relation (3), $\langle P_y\rangle$ increases linearly with the applied transverse field E_y, with a slope that is independent of the atom number N. Clearly, the data in Fig. 2 provide a direct verification of this predicted linear dependence (see also Supplementary Fig. S3). On the contrary, the longitudinal current $J_x(\tau)$ does not show a sensitive dependence on E_y (see Supplementary Fig. S2). Thus, we use the current $\langle J_x\rangle = \langle J_x(\tau)\rangle_{\tau,E_y}$, averaged over the same time interval $\tau \in [1, 5]$ considered for the determination of P_y, as well as over different values of transverse field E_y.

The linear fit of the experimental data in Fig. 2 allows us to determine the Hall field E_H – or, equivalently, the Hall voltage V_H – corresponding to $\langle P_y\rangle = 0$. The dependence of E_H with the total atom number N is shown in Fig. 3a (filled circles). The additional data points in Fig. 3a (empty circles) are also extracted from the data reported in Fig. 2, when fitting P_y as a function of N for different transverse field values E_y (see Supplementary Fig. S1). The data show a suppression of E_H with the total atom number N. Remarkably, the suppression of E_H

https://doi.org/10.1038/s41467-025-65083-6

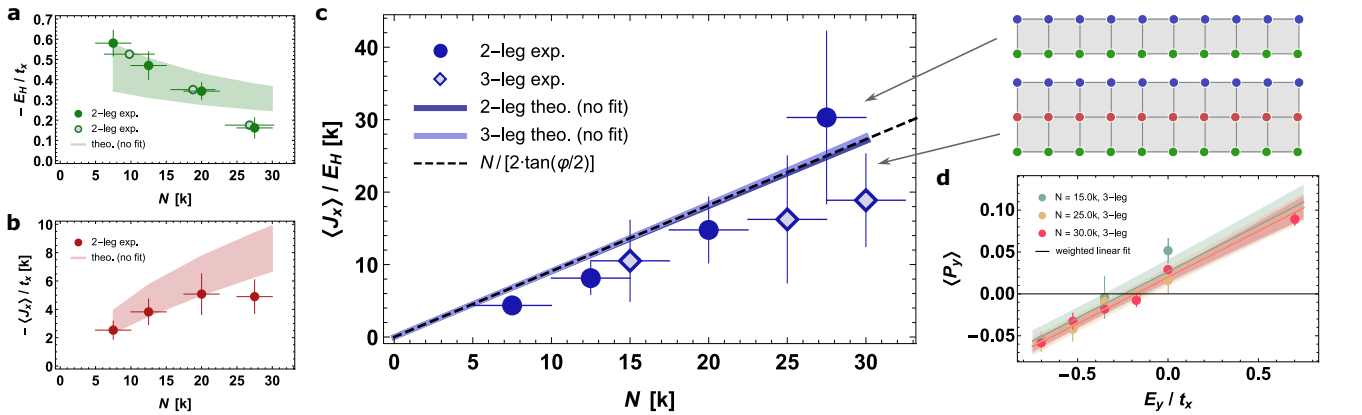

Fig. 3 | Dependence of the inverse Hall resistance on atom number and robustness with respect to ladder geometry. The data are measured in the single-band regime at $t_y = 3.30t_x$ and $U = 6.56t_x$. **a** Hall field E_H as a function of the atom number N for a two-leg ladder. The filled circles are obtained from the linear fit of the data in Fig. 2, and the vertical error bars represent the 95% confidence interval; the empty circles and their horizontal error bars are also extracted from the data reported in Fig. 2, when fitting P_y as a function of N for different transverse field values E_y. **b** Averaged current $\langle J_x \rangle$ as a function of the atom number N for a two-leg ladder. The vertical error bars denote the standard deviation of $\langle J_x \rangle = \langle J_x(\tau) \rangle_{\tau, E_y}$. **c** Inverse Hall resistance as a function of the atom number N for both two-leg (filled circles) and three-leg (empty diamonds) configurations. The dashed line indicates the universal relation of Eq. (4). The vertical error bars are obtained with standard uncertainty propagation. The horizontal error bars in **a** (filled circles), **b**, **c** indicate the range of atom number considered for each point. The colored areas in (**a**–**c**) are the numerical simulations from a mean-field approximation, accounting for the distribution of atom numbers in the tubes and experimental temperature uncertainty $1.5 \leq T/t_x \leq 3$. **d** The time-averaged Hall polarization $\langle P_y \rangle$ as a function of the transverse field E_y for three-leg ladders, with different total atom number $N = 15$ k, 25 k, and 30 k. The error bars denote the standard error of the mean, wherein the solid lines in corresponding colors are obtained from a weighted global linear fit with color shades representing the 95% confidence bands of the fit.

corresponds to the suppression of the longitudinal current per particle $\langle J_x \rangle / N$, which can be inferred from the sub-linear increase of $|\langle J_x \rangle|$ as N is increased, shown in Fig. 3b. A complete suppression is expected when the single conduction band is entirely filled and thus insulating.

These trends are well reproduced by theoretical simulations relying on a mean-field approximation of the interactions in Eq. (2), and reported as colored areas. As extensively discussed in ref. 27, the mean-field approximation has clear limitations in terms of quantitative accuracy, but it can account for the finite temperatures of the experiment ($T \simeq t_x$), which is much more challenging to address with exact studies. Moreover, P_y, J_x, and E_H are all non-universal quantities, which are sensitive to the microscopic details of the experiment, such as the exact distribution of the atoms in the tubes, their temperature, the shape of the drive, and confining potential. The width of the colored areas in Fig. 3 reflects the uncertainty on the temperature of the system, which is the experimental quantity with the highest uncertainty.

However, the fact that these quantities are intimately connected through the relation (3) puts strong constraints on their ratios, as it was previously shown for the Hall imbalance $\Delta_H = P_y/J_x$, which equals the universal value $2t_x \tan(\varphi/2)/t_y$ in the absence of a transverse compensation ($E_y = 0$)[27].

We now highlight the central result of our work, which emerges as a manifestation of the universality of transverse transport. We consider ρ_H, extracted from the ratio between the measured values of E_H and $\langle J_x \rangle$. Figure 3c illustrates the linear dependence of the inverse Hall resistance on the atom number. We observe that the experimentally measured $1/\rho_H$ exhibits a solid quantitative agreement with the theoretical prediction Eq. (4) (dashed line) for a large range of atom numbers, with no fitting parameters. We also find an almost perfect agreement with $1/\rho_H$ as extracted from numerical simulations (colored area), accounting for different tube average, finite temperatures, and confinement. Remarkably, the uncertainty on the temperature, responsible for a major broadening in the numerical prediction of E_H and $\langle J_x \rangle$, has almost no effect on $1/\rho_H$, reflecting the universal character of this latter quantity and its robustness against parameter changes. Our experimental observations testify to the robust and universal connection between the Hall resistance and the inverse carrier density $1/n$ in a strongly correlated single-band metal, stabilized in a two-leg ladder by strong on-rung repulsions.

We further demonstrate the universality of the relation between ρ_H and n by modifying the microscopic structure of the system and realizing a three-leg ladder configuration, where the Raman parameters were adjusted to extend the synthetic coupling to the $m_F = +3/2$ nuclear spin state (see Methods). The three-leg ladder features a similar trend of $\langle P_y \rangle$ to that of the two-leg case (see Fig. 3d). Thus, we determine E_H for the three-leg ladder with the same procedure as for the two-leg ladder and derive the corresponding inverse Hall resistance. Figure 3c compares the results of two-leg and three-leg ladders for different atom numbers. The measured data for the two configurations follow the same expected universal trend within experimental errors, in agreement with Eq. (4) and numerical simulations. The consistent relation between ρ_H and n in the two- and three-leg ladders confirms the effectiveness of our experimental procedure to measure the Hall resistance of a strongly correlated fermion system.

Discussion

In this experiment, we have established an efficient protocol to measure the Hall voltage in a fermionic cold-atom system. By employing simultaneous quenches of longitudinal and transverse fields, we have shown distinctive particle-density-dependent behavior of the Hall resistance in a controllable quantum simulator of Hall bars in ladder geometries threaded by a synthetic magnetic flux. These measurements demonstrate the universal relation between the Hall resistance and the number of carrier densities in strongly correlated single-band metals, with remarkable agreement with theoretical predictions.

The ability to measure the Hall voltage and the Hall resistance in clean and highly tunable cold-atom systems opens many exciting possibilities, including the direct comparison with the corresponding measurements in solid-state devices. It paves the way to the investigation of striking features of strongly correlated topological phases of matter, such as the quantization of the transverse resistance (the Hall plateau) with ultracold atoms, as well as the role of the interaction anisotropy. Furthermore, interesting perspectives reside in exploring the Hall resistivity of Mott insulating phases at low doping and at the metal to insulator transition[45], as well as measuring other Hall effects,

such as the thermal Hall one, where the current is induced by a temperature gradient[55].

Methods

Generation of effective magnetic and electric fields

The complex tunneling $t_y e^{i\varphi j}$ along the synthetic dimension in Eq. (2) is implemented by the coherent coupling between different spin states, via two Raman laser beams propagating with a relative angle. The different periodicity of the Raman coupling with respect to the lattice spacing d, gives rise to a non-zero Peierls phase $\varphi = (\Delta \vec{k} \cdot \hat{x})d$ with $\Delta \vec{k}$ denoting the wavevector of the coupling field, leading to a synthetic magnetic flux $\varphi = 0.32\pi$ piercing the ladder plaquettes.

The effective electric field E_x along the longitudinal direction is realized by shining a far-off-resonance red-detuned laser beam operating at 1112 nm. This laser is aligned in the way that the atomic cloud center is located at the maximum slope of the Gaussian beam profile, to ensure the induced light-shift gradient, which stems from the intensity gradient provided by the Gaussian beam, has sufficient linearity. In particular, the beam waist is 85 μm, and the variation of the expected Bloch frequency among central 40 lattice sites (estimated region of the atomic sample) is less than 3%.

The effective electric field E_y along the synthetic dimension is instead implemented by abruptly adding a small Raman laser detuning (−120 Hz ~ 120 Hz) after adiabatically loading the ground state of the system. To relate such a detuning to an energy difference along the synthetic dimension, consider the Hamiltonian describing the Raman coupling for a two-leg ladder in the rotating frame

$$H_R = \begin{pmatrix} 0 & t_y \\ t_y & -E_y \end{pmatrix}. \tag{5}$$

One can clearly see that the presence of a detuning on the diagonal terms directly translates into an energy shift for different spin states, namely, an energy variation in the synthetic dimension. The Hall voltage V_H is then directly proportional to the fine-tuned Hall field E_H, which is expressed as $V_H = -(M-1)E_H$ by accounting for the total number of legs M.

Initial state preparation

The ^{173}Yb atoms are initially polarized in the $|F = 5/2, m_F = -5/2\rangle$ hyperfine component of the electronic ground state with a typical temperature of 0.2–0.25 T_F, where T_F is the Fermi temperature. The atomic cloud is first loaded into the vertical optical lattice along the gravitational direction within 150 ms using an exponential intensity ramp. The optical dipole trap, where the atoms are initially confined, is subsequently switched off in 1 s. Two horizontal optical lattices are then ramped up in the same way as the vertical lattice. The vertical lattice depth is set to $15E_r$, where $E_r = h^2/8\,md^2$ is the recoil energy, h is the Planck constant, m is the atomic mass, and d is the lattice spacing. Two horizontal lattice depths are set to $15E_r$ and $4E_r$, respectively, between which the shallow one with lattice depth of $4E_r$ is along the $\hat{x}$-direction. Thus, the tunneling rate $t_x/\hbar$ ($2\pi \times 171$ Hz) along the fermionic tubes is much larger than the radial tunneling rates ($2\pi \times 12.96$ Hz), which ensures the dynamics are only allowed in the shallow lattice along longitudinal direction $\hat{x}$. These independent 1D fermionic tubes are characterized by an axial harmonic confinement with a trapping frequency of $2\pi \times 43$ Hz, which originates from the Gaussian intensity profiles of the 2D red-detuned lattice beams.

After the lattice loading procedure, we employ an adiabatic preparation sequence to slowly activate the tunnel coupling between the legs and produce the equilibrium state of a M-leg ladder, where the nuclear spins act as different sites along a synthetic dimension $\hat{y}$ and whose plaquettes are threaded by a synthetic magnetic flux φ. The Raman laser beams are switched on with an initial detuning $\delta_i = -10$ kHz and perform an exponential frequency sweep of the form

$$\delta(t) = \delta_i + (\delta_f - \delta_i)\left(\frac{1 - e^{-t/T_{tau}}}{1 - e^{-T_{adiab}/T_{tau}}}\right), \tag{6}$$

where δ_f is chosen to resonantly couple the two nuclear spin states $|m_F = -1/2\rangle$ and $|m_F = -5/2\rangle$, with the ramp duration $T_{adiab} = 30$ ms and $T_{tau} = 14$ ms. The adiabaticity of the whole process is verified experimentally by reversing the whole procedure to recover a spin-polarized Fermi gas.

The Raman beams couple up to three nuclear spin states $m_F = -5/2$, $-1/2$, and $+3/2$ via σ^+/σ^- Raman transitions. The atoms are subjected to a $B_0 = 153$ Gauss (real) magnetic field along the vertical direction, generating a linear Zeeman splitting $\Delta_Z = 31.6(7)$ kHz between adjacent nuclear spin components. The frequency difference between the two Raman beams is set to $2\Delta_Z$, and we exploit the polarization-dependent Raman-induced light shifts to switch between the two-leg and the three-leg ladder case[20]. For the two leg case, we implement a horizontal polarization for both Raman laser beams, relative to the vertical quantization axis defined by the magnetic field, i.e., in the spherical basis $\hat{\epsilon}_{2L} = (\hat{\epsilon}_+ + \hat{\epsilon}_-)/\sqrt{2}$. Having a purely horizontal polarization offsets the $|m_F = +3/2\rangle$ spin state and effectively isolates it from the dynamics, being its population at most a few percent. To instead realize a three leg ladder, all three states need to be resonantly coupled. This condition can be fulfilled by implementing a uniform polarization for both Raman beams, namely $\hat{\epsilon}_{3L} = (\hat{\epsilon}_+ + \hat{\epsilon}_- + \hat{\epsilon}_\pi)/\sqrt{3}$. Under this condition the light shifts are approximately the same for the three states, which are all substantially populated throughout the experiment. The Raman coupling strength has a slight asymmetry for different nuclear spin states in the three-leg configuration owing to the spin-dependent Clebsch-Gordan relations. However, because the experiment is performed in the universal single-band regime, the specific value of t_y has no significant impact on the experimental results.

Theoretical methods and comparison to experimental data

The universal expression Eq. (3) for the Hall response is obtained by performing the perturbative expansion of the polarization P_y to leading order in the longitudinal hopping t_x and in the transverse field E_y, and by assuming that the strong interactions ($U = 6.56t_x$) stabilize a single band metal (see Supplementary Fig. S4)[32,50].

The details of this lengthy, but straightforward calculation are given in the Supplementary Information, where we also discuss the mean-field approximation and its comparison with the experimental data.

Data availability

All the experimental and theoretical data presented in the figures of the main article and Supplementary Information are available for download from an open repository[56].

Code availability

The numerical codes used in this study are publicly accessible at https://github.com/michelefilippone/Measuring_Hall_voltage_and_Hall_resistance_in_an_atom-based_quantum_simulator_OPEN_SOURCE.

References

1. Ashcroft, N. W. & Mermin, N. D. *Solid State Physics* (Saunders College Publishing, 1976).
2. von Klitzing, K. The quantized Hall effect. *Rev. Mod. Phys.* **58**, 519 (1986).
3. Prange, R. E. & Girvin, S. M. *The Quantum Hall Effect*, 2nd ed. (Springer New York, 1989).
4. Yoshioka, D. *The Quantum Hall Effect*, 1st ed. (Springer Berlin, Heidelberg, 2002).
5. Popovic, R. S. *Hall Effect Devices*, 2nd ed. (CRC Press, 2003).

6. von Klitzing, K. Essay: quantum Hall effect and the new international system of units. *Phys. Rev. Lett.* **122**, 200001 (2019).
7. von Klitzing, K., Dorda, G. & Pepper, M. New method for high-accuracy determination of the fine-structure constant based on quantized Hall resistance. *Phys. Rev. Lett.* **45**, 494 (1980).
8. Tsui, D. C., Stormer, H. L. & Gossard, A. C. Two-dimensional magnetotransport in the extreme quantum limit. *Phys. Rev. Lett.* **48**, 1559 (1982).
9. Hasan, M. Z. & Kane, C. L. Colloquium: topological insulators. *Rev. Mod. Phys.* **82**, 3045 (2010).
10. Xiao, D., Chang, M.-C. & Niu, Q. Berry phase effects on electronic properties. *Rev. Mod. Phys.* **82**, 1959 (2010).
11. Chiu, C.-K., Teo, J. C. Y., Schnyder, A. P. & Ryu, S. Classification of topological quantum matter with symmetries. *Rev. Mod. Phys.* **88**, 035005 (2016).
12. Haldane, F. D. M. Nobel lecture: topological quantum matter. *Rev. Mod. Phys.* **89**, 040502 (2017).
13. Wen, X.-G. Choreographed entanglement dances: topological states of quantum matter. *Science* **363**, 834 (2019).
14. Goldman, N., Budich, J. C. & Zoller, P. Topological quantum matter with ultracold gases in optical lattices. *Nat. Phys.* **12**, 639 (2016).
15. Ozawa, T. & Price, H. M. Topological quantum matter in synthetic dimensions. *Nat. Rev. Phys.* **1**, 349 (2019).
16. Xiang, Z.-C. et al. Simulating Chern insulators on a superconducting quantum processor. *Nat. Commun.* **14**, 5433 (2023).
17. Aidelsburger, M. et al. Realization of the Hofstadter Hamiltonian with ultracold atoms in optical lattices. *Phys. Rev. Lett.* **111**, 185301 (2013).
18. Aidelsburger, M. et al. Measuring the Chern number of Hofstadter bands with ultracold bosonic atoms. *Nat. Phys.* **11**, 162 (2015).
19. Miyake, H., Siviloglou, G. A., Kennedy, C. J., Burton, W. C. & Ketterle, W. Realizing the Harper Hamiltonian with laser-assisted tunneling in optical lattices. *Phys. Rev. Lett.* **111**, 185302 (2013).
20. Mancini, M. et al. Observation of chiral edge states with neutral fermions in synthetic Hall ribbons. *Science* **349**, 1510 (2015).
21. Stuhl, B. K., Lu, H.-I., Aycock, L. M., Genkina, D. & Spielman, I. B. Visualizing edge states with an atomic Bose gas in the quantum Hall regime. *Science* **349**, 1514 (2015).
22. Tai, M. E. et al. Microscopy of the interacting Harper-Hofstadter model in the two-body limit. *Nature* **546**, 519 (2017).
23. Genkina, D. et al. Imaging topology of Hofstadter ribbons. *New J Phys.* **21**, 053021 (2019).
24. Mukherjee, B. et al. Crystallization of bosonic quantum Hall states in a rotating quantum gas. *Nature* **601**, 58 (2022).
25. Viebahn, K. et al. Interactions enable Thouless pumping in a non-sliding lattice. *Phys. Rev. X* **14**, 021049 (2024).
26. Léonard, J. et al. Realization of a fractional quantum Hall state with ultracold atoms. *Nature* **619**, 495 (2023).
27. Zhou, T.-W. et al. Observation of universal Hall response in strongly interacting fermions. *Science* **381**, 427 (2023).
28. Lunt, P. et al. Realization of a Laughlin state of two rapidly rotating fermions. *Phys. Rev. Lett.* **133**, 253401 (2024).
29. Impertro, A. et al. Strongly interacting Meissner phases in large bosonic flux ladders. *Nat. Phys.* **21**, 895 (2025).
30. Wang, C. et al. Realization of fractional quantum Hall state with interacting photons. *Science* **384**, 579 (2024).
31. Chalopin, T. et al. Probing chiral edge dynamics and bulk topology of a synthetic Hall system. *Nat. Phys.* **16**, 1017 (2020).
32. Greschner, S., Filippone, M. & Giamarchi, T. Universal Hall response in interacting quantum systems. *Phys. Rev. Lett.* **122**, 083402 (2019).
33. Girvin, S. M. *The Quantum Hall Effect: Novel Excitations and Broken Symmetries* 53–175 (Springer Berlin, 2002).
34. Lopatin, A., Georges, A. & Giamarchi, T. Hall effect and interchain magneto-optical properties of coupled Luttinger liquids. *Phys. Rev. B* **63**, 075109 (2001).
35. Kapitulnik, A., Kivelson, S. A. & Spivak, B. Colloquium: anomalous metals: failed superconductors. *Rev. Mod. Phys.* **91**, 011002 (2019).
36. Brinkman, W. F. & Rice, T. M. Hall effect in the presence of strong spin-disorder scattering. *Phys. Rev. B* **4**, 1566 (1971).
37. León, G., Berthod, C. & Giamarchi, T. Hall effect in strongly correlated low-dimensional systems. *Phys. Rev. B* **75**, 195123 (2007).
38. Auerbach, A. Hall number of strongly correlated metals. *Phys. Rev. Lett.* **121**, 066601 (2018).
39. Zotos, X., Naef, F., Long, M. & Prelovšek, P. Reactive Hall response. *Phys. Rev. Lett.* **85**, 377 (2000).
40. Lange, E. Memory-function approach to the Hall constant in strongly correlated electron systems. *Phys. Rev. B* **55**, 3907 (1997).
41. Shastry, B. S., Shraiman, B. I. & Singh, R. R. P. Faraday rotation and the Hall constant in strongly correlated Fermi systems. *Phys. Rev. Lett.* **70**, 2004 (1993).
42. Berg, E., Huber, S. D. & Lindner, N. H. Sign reversal of the Hall response in a crystalline superconductor. *Phys. Rev. B* **91**, 024507 (2015).
43. Citro, R., Giamarchi, T. & Orignac, E. Hall response in interacting bosonic and fermionic ladders. *Phys. Rev. Lett.* **134**, 056501 (2025).
44. Hagen, S. J., Lobb, C. J., Greene, R. L., Forrester, M. G. & Kang, J. H. Anomalous Hall effect in superconductors near their critical temperatures. *Phys. Rev. B* **41**, 11630 (1990).
45. Badoux, S. et al. Change of carrier density at the pseudogap critical point of a cuprate superconductor. *Nature* **531**, 210 (2016).
46. Smith, A. W., Clinton, T. W., Tsuei, C. C. & Lobb, C. J. Sign reversal of the Hall resistivity in amorphous Mo_3Si. *Phys. Rev. B* **49**, 12927 (1994).
47. Mihály, G., Kézsmárki, I., Zámborszky, F. & Forró, L. Hall effect and conduction anisotropy in the organic conductor $(TMTSF)_2PF_6$. *Phys. Rev. Lett.* **84**, 2670 (2000).
48. Moser, J. et al. Hall effect in the normal phase of the organic superconductor $(TMTSF)_2PF_6$. *Phys. Rev. Lett.* **84**, 2674 (2000).
49. Buser, M., Greschner, S., Schollwöck, U. & Giamarchi, T. Probing the Hall voltage in synthetic quantum systems. *Phys. Rev. Lett.* **126**, 030501 (2021).
50. Filippone, M., Bardyn, C.-E., Greschner, S. & Giamarchi, T. Vanishing Hall response of charged fermions in a transverse magnetic field. *Phys. Rev. Lett.* **123**, 086803 (2019).
51. Prelovšek, P., Long, M., Markež, T. & Zotos, X. Hall constant of strongly correlated electrons on a ladder. *Phys. Rev. Lett.* **83**, 2785 (1999).
52. Tusi, D. et al. Flavour-selective localization in interacting lattice fermions. *Nat. Phys.* **18**, 1201 (2022).
53. Taie, S. et al. Realization of a SU(2)SU(6) system of fermions in a cold atomic gas. *Phys. Rev. Lett.* **105**, 190401 (2010).
54. Huang, C.-H., Tezuka, M. & Cazalilla, M. A. Topological Lifshitz transitions, orbital currents, and interactions in low-dimensional Fermi gases in synthetic gauge fields. *New J. Phys.* **24**, 033043 (2022).
55. Melcer, R. A. et al. Heat conductance of the quantum Hall bulk. *Nature* **625**, 489 (2024).
56. Zhou, T.-W. et al. Datasets for "measuring Hall voltage and Hall resistance in an atom-based quantum simulator". *Zenodo* https://doi.org/10.5281/zenodo.17094135 (2025).

Acknowledgements

We gratefully acknowledge J. Mellado Muñoz for discussions and critical reading of the manuscript. For the experimental activity we acknowledge financial support by PNRR MUR project PE0000023-NQSTI financed by the European Union - Next Generation EU and by the Horizon Europe program HORIZON-CL4-2022-QUANTUM-02-SGA via the project 101113690 (PASQuanS2.1). This work is supported in part by the Swiss National Science Foundation under grant 200020_219400. M.F. acknowledges support from EPiQ ANR-22-PETQ-0007 part of Plan

France 2030. C.R. acknowledges support from ANR through Grant No. ANR-22-CE30-0022-01.

Author contributions

L.F., J.C., G.C., M.F., T.-W.Z. and T.G. conceived the experiments. T.-W.Z., T.B., G.M. and J.P. carried out the experimental work. T.-W.Z., T.B. and G.M. analyzed the experimental results. C.R., M.F., and T.G. performed theoretical work. All authors contributed extensively to the discussion of the results and to the writing of the manuscript.

Competing interests

The authors declare no competing interests.

Additional information

Supplementary information The online version contains supplementary material available at https://doi.org/10.1038/s41467-025-65083-6.

Correspondence and requests for materials should be addressed to L. Fallani.

Peer review information *Nature Communications* thanks the anonymous reviewer(s) for their contribution to the peer review of this work. A peer review file is available.

Reprints and permissions information is available at http://www.nature.com/reprints

Publisher's note Springer Nature remains neutral with regard to jurisdictional claims in published maps and institutional affiliations.

Open Access This article is licensed under a Creative Commons Attribution-NonCommercial-NoDerivatives 4.0 International License, which permits any non-commercial use, sharing, distribution and reproduction in any medium or format, as long as you give appropriate credit to the original author(s) and the source, provide a link to the Creative Commons licence, and indicate if you modified the licensed material. You do not have permission under this licence to share adapted material derived from this article or parts of it. The images or other third party material in this article are included in the article's Creative Commons licence, unless indicated otherwise in a credit line to the material. If material is not included in the article's Creative Commons licence and your intended use is not permitted by statutory regulation or exceeds the permitted use, you will need to obtain permission directly from the copyright holder. To view a copy of this licence, visit http://creativecommons.org/licenses/by-nc-nd/4.0/.

© The Author(s) 2025